Atmos. Meas. Tech., 10, 3133–3149, 2017
https://doi.org/10.5194/amt-10-3133-2017

Atmospheric Measurement Techniques
Open Access
EGU

The version 3 OMI NO_2 standard product

Nickolay A. Krotkov[1], Lok N. Lamsal[2,1], Edward A. Celarier[2,1], William H. Swartz[3,1], Sergey V. Marchenko[4,1], Eric J. Bucsela[5], Ka Lok Chan[6], Mark Wenig[6], and Marina Zara[7]

[1]Atmospheric Chemistry and Dynamics Laboratory, NASA Goddard Space Flight Center, Greenbelt, MD, USA
[2]GESTAR, Universities Space Research Association, Columbia, Maryland, USA
[3]Applied Physics Laboratory, Johns Hopkins University, Laurel, Maryland, USA
[4]Science Systems and Applications, Inc., Lanham, Maryland, USA
[5]SRI International, Menlo Park, California, USA
[6]Department of Physics, Ludwig Maximilian University, Munich, Germany
[7]Royal Netherlands Meteorological Institute (KNMI), De Bilt, the Netherlands

Correspondence to: Nickolay A. Krotkov (nickolay.a.krotkov@nasa.gov)

Received: 12 February 2017 – Discussion started: 24 March 2017
Revised: 24 March 2017 – Accepted: 24 July 2017 – Published: 1 September 2017

Abstract. We describe the new version 3.0 NASA Ozone Monitoring Instrument (OMI) standard nitrogen dioxide (NO_2) products (SPv3). The products and documentation are publicly available from the NASA Goddard Earth Sciences Data and Information Services Center (https://disc.gsfc.nasa.gov/datasets/OMNO2_V003/summary/). The major improvements include (1) a new spectral fitting algorithm for NO_2 slant column density (SCD) retrieval and (2) higher-resolution (1° latitude and 1.25° longitude) a priori NO_2 and temperature profiles from the Global Modeling Initiative (GMI) chemistry–transport model with yearly varying emissions to calculate air mass factors (AMFs) required to convert SCDs into vertical column densities (VCDs). The new SCDs are systematically lower (by ∼ 10–40 %) than previous, version 2, estimates. Most of this reduction in SCDs is propagated into stratospheric VCDs. Tropospheric NO_2 VCDs are also reduced over polluted areas, especially over western Europe, the eastern US, and eastern China. Initial evaluation over unpolluted areas shows that the new SPv3 products agree better with independent satellite- and ground-based Fourier transform infrared (FTIR) measurements. However, further evaluation of tropospheric VCDs is needed over polluted areas, where the increased spatial resolution and more refined AMF estimates may lead to better characterization of pollution hot spots.

1 Introduction

Emissions and concentrations of nitrogen oxides ($NO_x = NO + NO_2$) are regulated in several countries, as nitrogen dioxide (NO_2) is a toxic pollutant (US EPA, 2017) and NO_x leads to the formation of surface-level ozone, acid rain, and particular matter (Seinfeld and Pandis, 1998). NO_x also indirectly impacts climate through the formation of free-tropospheric ozone (Jacob et al., 1996), a greenhouse gas, and secondary aerosols that scatter solar radiation and cool Earth's surface (Shindell et al., 2009). Major sources of NO_x include fuel combustion, soil, and lightning.

Away from sources of tropospheric pollution, nearly 90 % of the NO_2 total vertical column density (VCD) is found in the stratosphere. There, it is approximately zonally symmetric and varies meridionally with season. Stratospheric NO_2 is produced primarily by the oxidation of nitrous oxide (N_2O) transported from the troposphere. It catalytically destroys ozone and suppresses ozone loss by other catalytic mechanisms through the sequestration of active radical species (Seinfeld and Pandis, 1998).

NO_2 has strong spectral absorption lines in the visible (Vis) and near-ultraviolet (UV) range, which permit its measurement by remote-sensing techniques. A new generation of spectroscopic ground-based instruments can measure total (Herman et al., 2009) and tropospheric (Hönninger et al., 2004; Spinei et al., 2014) NO_2 columns at high temporal resolution. The first space-based NO_2 observations started

in the mid-1990s with the Global Ozone Monitoring Experiment (GOME) instrument (Burrows et al., 1999; Martin et al., 2002; Richter et al., 2005). Similar measurements, but at higher spatial resolution, continued with the SCanning IMaging spectrometer for Atmospheric CHartographY (SCIAMACHY: 2002–2012; Bovensmann et al., 1999), the Ozone Monitoring Instrument (OMI: 2004–present; Levelt et al., 2006a, b), and GOME-2 (2006–present; Callies et al., 2000; Valks et al., 2011). Of these, OMI offers the highest spatial resolution, longest record, and least instrument degradation (Dobber et al., 2008; Marchenko and DeLand, 2014; Schenkeveld et al., 2017).

Satellite NO_2 data have been used as a proxy for (1) NO_x emissions (van der A et al., 2017; Beirle et al., 2011; Boersma et al., 2015; Castellanos and Boersma, 2012; Curier et al., 2014; Ding et al., 2015; Duncan et al., 2014, 2016, de Foy et al., 2014, 2015, 2016; Ghude et al., 2013; Jaeglé et al., 2004; Konovalov et al., 2006, 2010; Lamsal et al., 2011; Liu et al., 2016; Lu et al., 2015; Lu and Streets, 2012; Martin et al., 2006; McLinden et al., 2016; Mijling and Van Der A, 2012; Richter et al., 2004, 2005; Russell et al., 2012; Stavrakou et al., 2008; Streets et al., 2013; Vinken et al., 2014; Zhang et al., 2007; Zhou et al., 2012); (2) ground-level NO_2 (Lamsal et al., 2008) and NO_2 deposition (Nowlan et al., 2014); and (3) emissions of co-emitted gases, including other pollutants, like particulate matter, and greenhouse gases, such as CO_2 (Berezin et al., 2013; Konovalov et al., 2016; Reuter et al., 2014).

There are two operational OMI NO_2 products: the NASA standard product (SP) (Bucsela et al., 2013; Lamsal et al., 2014) and the Dutch OMI NO_2 (DOMINO), produced by the Royal Netherlands Meteorological Institute, KNMI (Boersma et al., 2011). Both products use the differential optical absorption spectroscopy (DOAS) spectral fitting approach (Platt and Stutz, 2008) to derive NO_2 slant column density (SCD), which represents the total NO_2 amount (molecules cm^{-2}) along the average solar radiation path through the atmosphere as observed from OMI. After separation of tropospheric and stratospheric SCDs, these are converted to the respective NO_2 VCDs using model-derived air mass factors (AMFs): $\mathrm{VCD} = \mathrm{SCD}/\mathrm{AMF}$. The previous NASA algorithm (version SPv2) used the same NO_2 SCDs as DOMINO v2 (Boersma et al., 2011), employing different approaches to the stratosphere–troposphere separation (STS) and AMF calculation (Bucsela et al., 2013). Both products were in general agreement and produced similar regional trends in tropospheric VCDs (Krotkov et al., 2016), but comparison of OMI stratospheric NO_2 VCDs (SPv2 and DOMINO v2) with other independent measurements revealed that they were overestimated by as much as 40 % over unpolluted regions (Belmonte Rivas et al., 2014). The overestimation was traced to the common DOAS retrieval step (Van Geffen et al., 2015; Marchenko et al., 2015).

This paper describes the new OMI operational NO_2 standard product, version 3 (SPv3), which is available from the NASA Goddard Earth Sciences Data and Information Services Center (GES DISC: https://disc.gsfc.nasa.gov/datasets/OMNO2_V003/summary/). For version 3, we have developed a new DOAS spectral fitting algorithm, described in Sect. 3, which has brought OMI NO_2 SCDs and inferred VCDs into much better agreement with independent satellite- and ground-based measurements and with model simulation results (Marchenko et al., 2015). Other changes include the use of higher-spatial-resolution a priori NO_2 profiles from the Global Modeling Initiative (GMI) chemistry and transport model (CTM), with updated, year-dependent emissions (Strode et al., 2015) and new higher-resolution temperature profiles and tropopause height from the NASA Modern-Era Retrospective Analysis for Research and Applications (MERRA) model (Rienecker et al., 2011), discussed in Sect. 2. Sections 4 and 5 compare the SPv3 with the previous version and with ground-based and satellite data.

2 Observations and model climatology

2.1 OMI measurements

The OMI instrument (Levelt et al., 2006b) on the Earth Observing System Aura satellite (Schoeberl et al., 2006) is a push broom UV–Vis spectrometer that measures the Earth's backscattered radiance and solar irradiance. The EOS Aura satellite is flying in a sun-synchronous polar orbit with an Equator-crossing time of about 13:45 local time (ascending node). The swath width of OMI is 2600 km, enabling global daily coverage with a nadir field-of-view (FOV) size of 13 km × 24 km (along track × across track). OMI measurements have been radiometrically stable, as evidenced by regular evaluations of the instrument sensitivity changes (Dobber et al., 2008; Marchenko and DeLand, 2014; Schenkeveld et al., 2017). Comprehensive monitoring of the instrument's mission-long performance shows less than 3 % degradation in radiances and irradiances in the 400–470 nm spectral range, stable long-term wavelength registration ($\Delta\lambda \sim 0.002$ nm, with ~ 0.001 nm seasonal fluctuations), stable instrument slit function (~ 0.1 %), and stable stray-light contamination in radiance and irradiance (~ 0.5 % in the visible range; Schenkeveld et al., 2017). These qualities ensure generation of a consistent, long-term data record of NO_2 needed for the estimation of global trends, emissions, and other applications. Beginning in 2007, radiance measurements in some FOVs have been affected, apparently by a physical blockage of the entrance optics, rendering those measurements useless; this is called the "row anomaly" (Dobber et al., 2008). Rejection of the anomalous FOVs leads to complete global coverage in 2 days instead of one, as before the row anomaly.

2.2 GMI model

Calculation of the AMF relies on an a priori NO_2 profile shape. The SPv3 AMF calculation uses the GMI three-dimensional CTM simulation in the troposphere and stratosphere (Duncan et al., 2007; Strahan et al., 2013). The GMI CTM uses a stratosphere–troposphere chemical mechanism, natural and anthropogenic emissions, and aerosol fields from the Goddard Chemistry Aerosol Radiation and Transport (GOCART) model (Chin et al., 2014). It simulates tropospheric processes such as NO_x production by lightning, scavenging, and wet and dry deposition. Meteorological fields, including temperature profile and tropopause pressure, are the results of MERRA and have 72 levels from the surface to 0.01 hPa with a resolution ranging from $\sim$ 150 m in the boundary layer to $\sim$ 1 km in the upper troposphere and lower stratosphere. GMI simulations with MERRA have been evaluated in the troposphere and stratosphere. Strode et al. (2015) showed good agreement with tropospheric O_3 and NO_x trends in the US in a 1990–2013 hindcast simulation. Strahan et al. (2016) demonstrated realistic seasonal and interannual variability of Arctic composition using comparisons to Aura Microwave Limb Sounder (MLS) O_3 and N_2O. We have found GMI's NO_2 simulation in both the troposphere (Lamsal et al., 2015) and stratosphere (Spinei et al., 2014; Marchenko et al., 2015) to be in good agreement with observations.

As in SPv2, the a priori profiles for SPv3 are monthly means of daily GMI profiles, sampled at the OMI overpass time (13:00–14:00 local time). The changes in the GMI simulation are summarized in Table 1. Galactic cosmic rays (GCRs) were added to the model as an important source of stratospheric NO_x at high latitudes. The NO photodissociation rate, j(NO), was reduced by 40 %, consistent with recent recommendations (M. Prather, personal communication, 2016), in part based on a discrepancy between a related model and balloon measurements of NO_y (Hsu and Prather, 2010). As NO photodissociation leads to loss of NO_x in the stratosphere, reduction of j(NO) increases stratospheric NO_2 relative to the GMI simulation used in SPv2.

3 Algorithm description

As mentioned before, the SPv3 algorithm makes important improvements to the SPv2 approach, including a new OMI-optimized DOAS spectral fit to determine SCDs (S) and the improvement of AMFs for both the stratosphere and troposphere (A_{strat} and A_{trop}). The STS algorithm remains unchanged from Bucsela et al. (2013). The main steps are depicted in Fig. 1 and described in more detail in the following subsections.

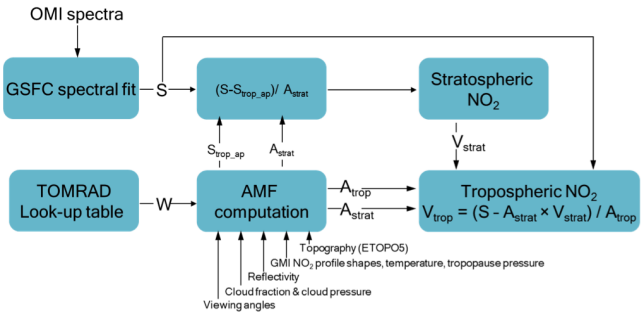

Figure 1. Schematic description of the OMI NO_2 processing algorithm. S variables represent slant column densities (SCDs); A represents air mass factors (AMFs). V variables represent vertical column densities (VCDs). $\boldsymbol{W}$ denotes the scattering weight (Eq. 1), pre-computed using the radiative transfer program TOMRAD.

3.1 New SCD retrieval

In the new spectral fitting approach (Marchenko et al., 2015), we address certain shortcomings of the conventional DOAS approach, as applied to OMI retrievals. Conventional DOAS relies on very precise wavelength calibration and simultaneously determines the trace gas absorptions and magnitude of the inelastic rotational Raman (RR) scattering effect (Chance and Spurr, 1997; Grainger and Ring, 1962; Joiner et al., 1995). However, it is quite sensitive to the selection of the spectral fitting window; to the order of the closure polynomial; and, most of all, to even a slight misregistration between the radiance and irradiance wavelengths. We apply a multi-step, iterative – rather than simultaneous – retrieval procedure for all interfering species in the broad spectral window from 402 to 465 nm.

Due to the statistical characteristics of the individual OMI solar irradiance measurements (Marchenko and DeLandm 2015), we use monthly-averaged, rather than daily, solar spectra. The monthly-averaged solar spectra will not capture the daily solar variability, which may differ by about 0.1 % around 430 nm and < 0.05 % elsewhere.

In most spectral measurements, the RR effect imposes by far the largest signal in the spectral reflectances (radiance/irradiance). Our first step is to use the spectral structure of the RR signal to (1) ascertain and correct the wavelength offset between radiance and irradiance ($\sim$ 0.002 nm; cf. with the 0.21 nm spectral sampling step) and (2) remove the RR signal prior to estimating the SCDs. We assess the wavelength dependence of the shifts by splitting the entire fitting window into multiple overlapping micro-window segments and evaluating the RR spectrum amplitudes and wavelength adjustments for each segment. To account for the RR line-filling patterns, we use a linear combination of the atmospheric (Joiner et al., 1995) and the liquid-water (Vasilkov, 2002) RR spectra, convolved with the wavelength- and cross-track-dependent OMI spectral transfer function (Dobber et al., 2006).

Table 1. GMI model specifications used in SP NO_2 retrieval.

Model parameter	SPv2.1 (released 2012)	SPv3.0 (released 2016)
Spatial resolution (lat × lon)	2° × 2.5°	1° × 1.25°
Meteorological fields	GEOS5.1	MERRA
Fossil fuel NO_x emissions	Constant 2005–7	Time-dependent
Biomass burning NO_x emissions	Constant 2005–7	Time-dependent
Lightning NO_x coefficients	Calculated from 2005–2007 of older simulation	Calculated from over 20 years of MERRA reanalysis
Tropospheric aerosols	Constant year 2001 GOCART	Time-dependent GOCART
Stratospheric aerosols	Constant year 2000	Time-dependent (IGAC)
Galactic cosmic rays	No	Yes
j(NO) scaling factor	1.0	0.6

Other steps in the algorithm include the estimation of, and correction for, spectral under-sampling patterns (Chance et al., 2005) and aggressive suppression of instrumental noise.

3.2 AMF calculation

The method of AMF calculation remains the same as in SPv2 (Bucsela et al., 2013), which agrees well with independent estimates (Lorente et al., 2017). To calculate stratospheric and tropospheric AMFs, we use a pre-computed dimensionless scattering weight vector $\boldsymbol{W}$ (also known as the Box-AMF; Platt and Stutz, 2008). $\boldsymbol{W}$ describes the relationship between S for a column (stratospheric or tropospheric) and the local VCD, V_i, in each atmospheric layer i within the column (Palmer et al., 2001; Martin et al., 2002):

$$S = \sum_i \boldsymbol{W}_i \times V_i = A \times \sum_i V_i = A \times V. \quad (1)$$

$\boldsymbol{W}$ is pre-computed using the radiative transfer program TOMRAD (Dave, 1965), accounting for multiple molecular (Rayleigh) scattering in an atmosphere bounded by a Lambertian surface. Since the Lambertian equivalent surface reflectance (LER) is assumed to be wavelength-independent, $\boldsymbol{W}$ varies smoothly with wavelength (within ∼ 20 %) across the NO_2 fitting window. Therefore, we calculate a single $\boldsymbol{W}$ vector, representative of the entire spectral fitting window, which is stored in a lookup table (Bucsela et al., 2013). Stratospheric and tropospheric AMFs are calculated, separated at the climatological MERRA monthly tropopause pressure (i.e., A_{trop} and A_{strat} in Fig. 1). In the stratosphere, $\boldsymbol{W}$ is approximately constant with altitude and is determined by the solar and viewing zenith angles: $\boldsymbol{W}_{i,\text{strat}} \approx \sec(\text{SZA}) + \sec(\text{VZA})$. In the free troposphere, $\boldsymbol{W}_{i,\text{trop}}$ increases with altitude and strongly depends on the cloud radiance fraction and optical centroid pressure (Sneep et al., 2008; Stammes et al., 2008; Vasilkov et al., 2009). In the boundary layer and under cloud-free conditions, $\boldsymbol{W}$ depends most strongly on altitude and surface pressure and reflectance (Vasilkov et al., 2017).

The AMF for a stratospheric or tropospheric column is computed as the vertical integral of the NO_2 profile shape weighted average of $\boldsymbol{W}$ (Eq. 1) using the a priori profiles described in Sect. 2.2. These profiles capture the interannual (Lamsal et al., 2015) and seasonal (Lamsal et al., 2010) variability of the AMF. The SPv3 uses yearly varying monthly mean NO_2 profiles from 2004 to 2014. For dates starting in 2015, the 2014 monthly profiles are used. The $\boldsymbol{W}$ is corrected for the monthly mean GMI temperature profile as described in Bucsela et al. (2013), since the S retrieval algorithm relies on a constant temperature (220 K) NO_2 cross sections. We provide $\boldsymbol{W}$ to allow users to derive their own estimates of AMFs and VCDs using their own a priori NO_2 profiles, for example from another model or observations.

OMI NO_2 column averaging kernels (**AK**s) can be calculated from the $\boldsymbol{W}$ and corresponding AMFs for stratospheric or tropospheric columns: $\mathbf{AK} = \mathrm{d}V/\mathrm{d}V_i = \boldsymbol{W}/\mathrm{A}$ (Eskes and Boersma, 2003). The **AK**s are used in data assimilation, observational system simulation experiments, and comparisons with vertically resolved measurements and CTM models.

3.3 Stratosphere–troposphere separation

The STS algorithm remains the same as in the previous version (Bucsela et al., 2013), which shows overall good agreement with the independent STRatospheric Estimation Algorithm from Mainz (STREAM) – a verification algorithm for the Sentinel-5 Precursor TROPOspheric Monitoring Instrument (TROPOMI) STS (Beirle et al., 2016). The V_{strat} and V_{trop} are retrieved separately under the assumption that the two are largely independent (Fig. 1). The stratospheric field is computed first, beginning with creation of a gridded global initial field $V_{\text{init}} = S/A_{\text{strat}}$, assembled from data taken within ±7 orbits of the target orbit. An a priori estimate of the tropospheric contribution to this field, $S_{\text{trop\_ap}}/A_{\text{strat}}$, based on a monthly GMI model climatology and OMI cloud measurements is subtracted, and the potentially contaminated grid cells where this contribution exceeds 0.3×10^{15} molec. cm^{-2} are masked. A three-step (interpolation, filtering, and smoothing) algorithm (Bucsela et al., 2013) is then applied to fill in the masked regions and data gaps and to remove residual tropospheric contamination. The resulting stratospheric vertical column field V_{strat} is converted to a slant column field using A_{strat} and subtracted

Table 2. SP NO_2 retrieval biases and noise estimated over unpolluted, mostly cloud-free (cloud radiance fraction < 0.3) Pacific Ocean regions in July 2011 ($\times 10^{15}$ molec. cm^{-2}).

Parameter	SPv2.1 (released 2012)	SPv3.0 (released 2016)
Bias in S	max(1.2, 0.1 × S)[1]	±0.5[2]
Noise in S	0.8 ± 0.2[3]	0.9 ± 0.3[4]
Bias in $V_{init} = S/A^5_{strat}$	+0.60	±0.25
Noise in $V_{init} = S/A^5_{strat}$	0.40 ± 0.10	0.45 ± 0.15
Bias in V_{strat}	+0.6[6]	< 0.3[7]
Noise in V^8_{strat}	0.10 ± 0.04	0.10 ± 0.03
Bias in V^9_{trop}	±0.1	−0.1
Noise in V^{10}_{trop}	0.36 ± 0.03	0.45 ± 0.04

[1] Estimated as constant offset value ∼ 1.2 (Van Geffen et al., 2015) for $S < 12 \times 10^{15}$ molec. cm^{-2} and multiplicative value ∼ 0.1 × S for $S > 12 \times 10^{15}$ molec. cm^{-2} (Marchenko et al., 2015). [2] Intercomparison of independent DOAS fitting algorithms (Zara et al., 2016). [3–4] Mission time average value of standard deviation in S over Pacific regions in 2011; upper limit corresponds to small S. The noise increased by ∼ 20 % during OMI mission: from ∼ 0.8 × 10^{15} molec. cm^{-2} in 2005 to ∼ 1.0 × 10^{15} molec. cm^{-2} in 2016 (Zara et al., 2016). [5] Upper limit of uncertainty in V_{int} is estimated from uncertainties in S assuming $A_{strat} \sim 2$. [6] Relative to satellite limb observations (Belmonte Rivas et al., 2014). [7] Comparisons with independent satellite- and ground-based Fourier transform infrared (FTIR) measurements at Izana. [8] Estimated as the standard deviation of V_{strat} over the tropical South Pacific region (5 to 15° S and 130 to 160° W) in 2011. Uncertainty reflects noise seasonal dependence (Fig. 2). [9] Estimated as the difference between mean OMI retrieved and a priori bias = < V_{trop} > − < V_{trop_ap} > over unpolluted homogeneous tropical South Pacific region. [10] Estimated as the standard deviation of V_{trop} over the tropical South Pacific region (5 to 15° S and 120 to 160° W) in 2011. Uncertainty reflects noise seasonal dependence (Fig. 2).

from the measured S to provide S_{trop}, leading to the desired $V_{trop} = S_{trop}/A_{trop}$ (Fig. 1). As discussed in Sect. 3.2, the S_{trop} can be combined with independently calculated A_{trop} to develop customized regional V_{trop} products, for example, using higher-spatial-resolution a priori information (Goldberg et al., 2017; Kuhlmann et al., 2015; Laughner et al., 2016; Lin et al., 2014; Russell et al., 2011, 2012).

3.4 Retrieval noise and bias

We compare noise and biases in SPv2 and SPv3 by analyzing retrievals over homogeneous unpolluted Pacific regions with negligible tropospheric contribution (Fig. 2). The data are filtered to minimize geophysical, observational, and cloud-induced variability. The selection criteria result in low SCDs with the largest DOAS fitting uncertainties and should be treated as upper bounds on uncertainties over unpolluted, mostly cloud-free regions (Table 2). In this relatively clean region, uncertainties in the AMF and STS are much smaller than in polluted regions, where (1) the tropospheric column is much larger than the stratospheric column and (2) the STS algorithm is filling in where data were masked (Beirle et al., 2016; Bucsela et al., 2013).

Our new OMI DOAS spectral fitting algorithm (Marchenko et al., 2015) greatly reduces the positive biases (i.e., constant offset in $S \sim +1.2 \times 10^{15}$ molec. cm^{-2} and multiplicative factor 0.1 × S) in the previous version, albeit with slightly increased noise ($0.9 \pm 0.3 \times 10^{15}$ molec. cm^{-2}, Table 2). We estimate the noise as a standard deviation of the mostly cloud-free S retrievals over nearly homogeneous Pacific regions. The upper limit corresponds to the tropical regions and near-nadir observations, while the lower limit corresponds to large solar and/or OMI zenith angles (i.e., large S). The noise increased ∼ 20 % with time: from $\sim 0.8 \pm 0.3 \times 10^{15}$ molec. cm^{-2} in 2005 to $\sim 1.0 \pm 0.3 \times 10^{15}$ molec. cm^{-2} in 2015.

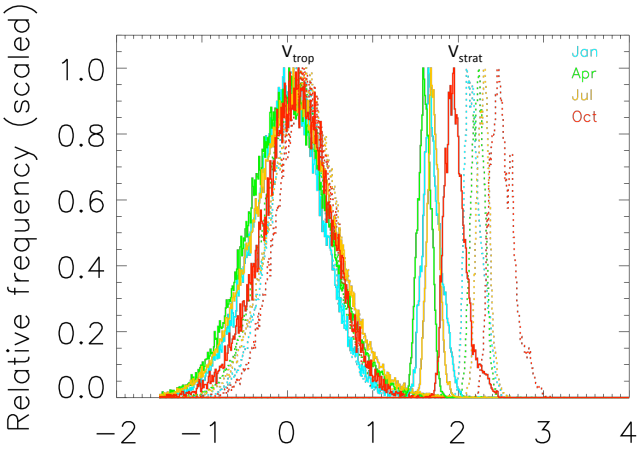

Figure 2. Probability distribution functions (PDFs) of the new SPv3 (solid lines) and previous version SPv2 (dashed lines) VCDs ($\times 10^{15}$ molec. cm^{-2}) retrieved in the Pacific region 15° S < lat < 5° S and 160° E < lon < 130° W during 2011. The width of the V_{trop} is used as proxy for estimated noise in $V_{trop} \sim 0.5 \times 10^{15}$ molec. cm^{-2} (Table 2).

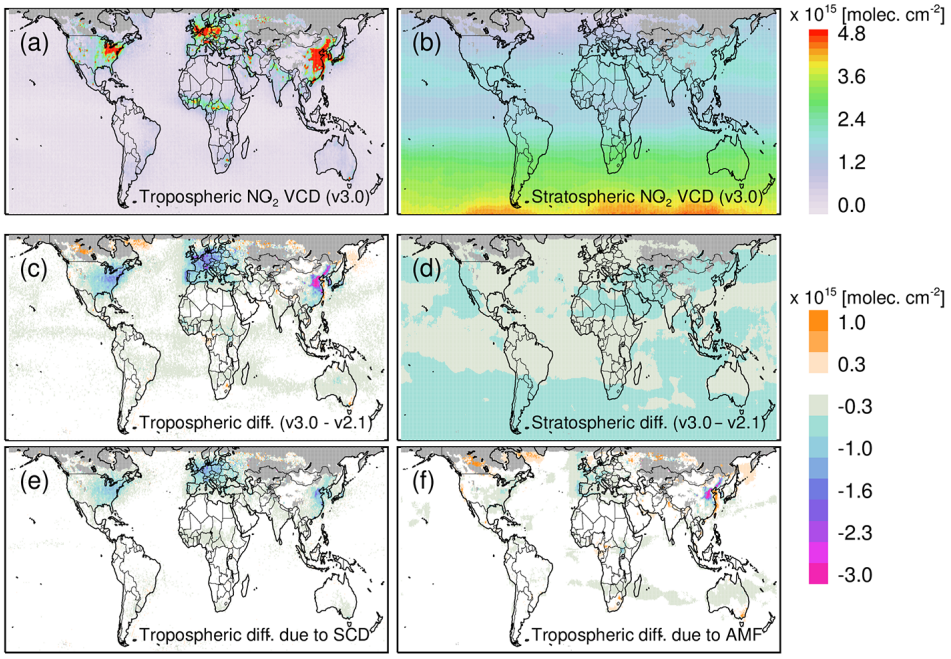

Figure 3. OMI NO_2 maps **(a, b)** and difference maps **(c, d)** for December 2006: tropospheric VCD (V_{trop}: **a, c**) and stratospheric VCD (V_{strat}: **b, d**). Bottom row: change in V_{trop} due to new SCD only **(e)**, and change in V_{trop} due to new a priori NO_2 profile shapes only **(f)**. Similar maps for July 2006 are shown in Supplement Fig. S1.

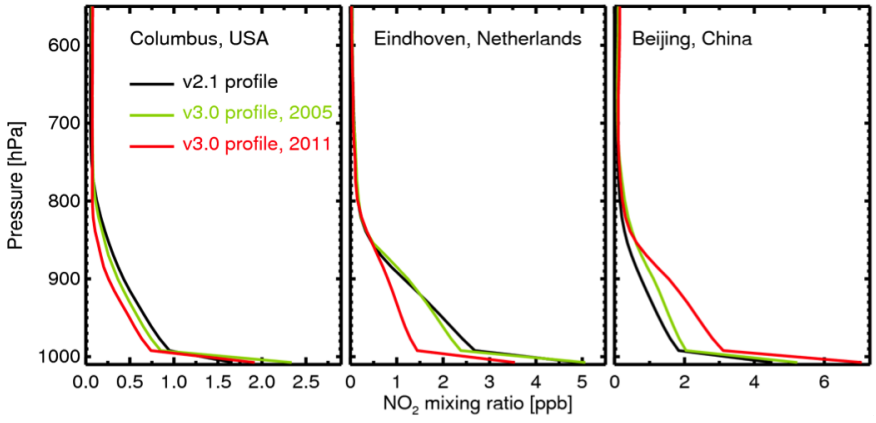

Figure 4. Monthly-averaged vertical distribution of NO_2 in July from GMI over selected locations in the eastern US, western Europe, and China. The color lines show the average NO_2 profiles derived from the new high-resolution ($1^\circ \times 1.25^\circ$) GMI simulation for 2005 (green) and 2011 (red). The black line shows NO_2 profiles derived from previous (SPv2) GMI simulation at $2^\circ \times 2.5^\circ$.

Figure 2 compares probability distribution functions (PDFs) of retrieved V_{strat} and V_{trop} derived by both versions over the equatorial South Pacific region for 4 months in 2011. As expected, the known overestimation in V_{strat} is reduced by a constant offset $\sim 0.6 \times 10^{15}$ molec. cm^{-2} in the new retrievals, bringing them into closer agreement with independent satellite (Adams et al., 2016; Belmonte Rivas et al., 2014; Marchenko et al., 2015) and ground-based FTIR measurements (Sect. 5). The noise in V_{strat}, estimated as standard deviation of the V_{strat} spatial distribution over the region 15° S < latitude < 5° S and 160° E < longitude < 130° W for each month, is unchanged from the previous version (Table 2). It is much lower than the upper-bound estimate of the noise in $V_{init} = S/2 \sim 0.45 \pm 0.15 \times 10^{15}$ molec. cm^{-2}, which is a result of the smoothing step in the STS algorithm (Bucsela et al., 2013).

The noise in $V_{trop} \sim 0.45 \pm 0.04 \times 10^{15}$ molec. cm^{-2} (Table 2) is estimated using its monthly standard deviation (Fig. 2). It is consistent with the upper bound of the noise in $V_{init} = S/A_{strat}$ assuming near-nadir observations and

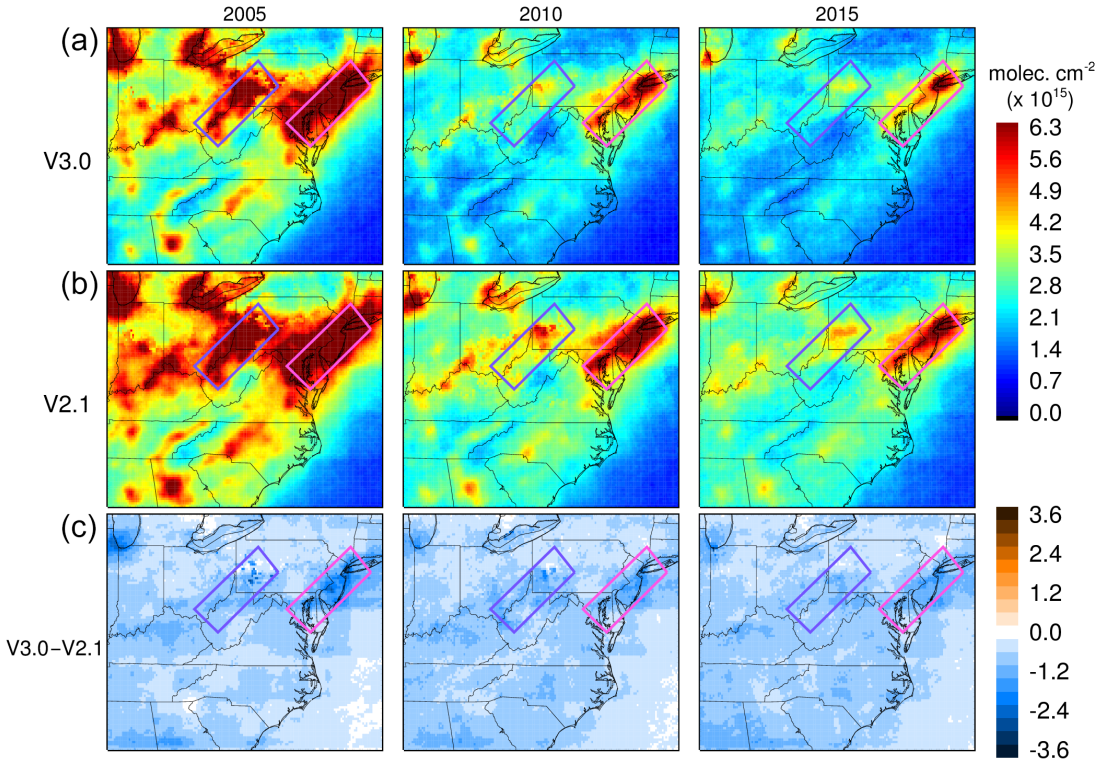

Figure 5. Annual average OMI NO_2 V_{trop} maps over the eastern US for 2005, 2010, and 2015: SPv3 **(a)**, SPv2 **(b)** and the difference: SPv3 – SPv2 **(c)**. The blue box outlines the Ohio River valley and southwestern Pennsylvania region with the predominant emissions from coal-fired power plants (Ohio in Fig. 6). The red box outlines the megalopolis from Washington, DC to New York along the I-95 interstate highway (I-95 corridor in Fig. 6) with predominant emissions from mobile sources. The regions have been discussed in Krotkov et al. (2016).

$A_{strat} \sim 2$. The deviation of the mean V_{trop} from $V_{trop-ap}$ is less than 0.1×10^{15} molec. cm^{-2}, as is expected given how the STS algorithm works (Bucsela et al., 2013).

Over polluted regions the "bias" in V_{trop} is poorly defined, as (1) it may be larger and more variable (Fig. 3) due to the larger spatiotemporal variability in tropospheric VCDs; (2) the A_{trop} is computed using OMI retrieved cloud pressures/fractions, climatological coarse-resolution surface reflectivities, and model-based monthly mean profiles, which may not accurately represent the true AMF (Lorente et al., 2017); and (3) the STS procedure fills in the stratospheric field over polluted regions using measurements from some distance away (Beirle et al., 2016; Bucsela et al., 2013).

The noise can be reduced with time averaging, e.g., creating monthly, seasonal, and annual average V_{trop}. Pixel averaging techniques, such as oversampling and pixel rotation along wind direction, have been developed to increase effective spatial resolution and signal-to-noise ratio, leading to improved detection and characterizations of point emission sources (Fioletov et al., 2015; de Foy et al., 2015; Kuhlmann et al., 2014; Lu et al., 2015; McLinden et al., 2016).

4 Comparison with previous version

Figure 3 shows global monthly mean V_{strat} and V_{trop} maps and difference maps from the previous SPv2 for December 2006, when we see the largest differences between the versions. The SPv3 V_{strat} is uniformly reduced by $0.5–0.8 \times 10^{15}$ molec. cm^{-2}. One notices very large reductions in V_{trop} ($\sim 2–5 \times 10^{15}$ molec. cm^{-2}) over heavily polluted regions in Europe; the eastern US; and, particularly, eastern China. However, for exceedingly large $V_{trop} > 10^{16}$ molec. cm^{-2} the relative difference between the two versions is usually less than $\sim 20\,\%$. The reductions in V_{trop} are smaller in other seasons (see Supplement Fig. S1 for July 2006). The V_{trop} reductions are caused by combined effects of smaller SCD (Fig. 3e) and changes in the updated emissions and spatial resolution of the a priori NO_2 profile shapes (Fig. 3f). All these changes reduce V_{trop} over most polluted areas of the world. By capturing the year-to-year changes in NO_2 profile shapes (Fig. 4), the updated emissions used in the new GMI simulation substantially change the NO_2 vertical distribution in the highly polluted regions, lending more confidence to the observed rapid changes in NO_2 around the globe in the last decade (Krotkov et al., 2016). These changes reflect a considerable decline in NO_x

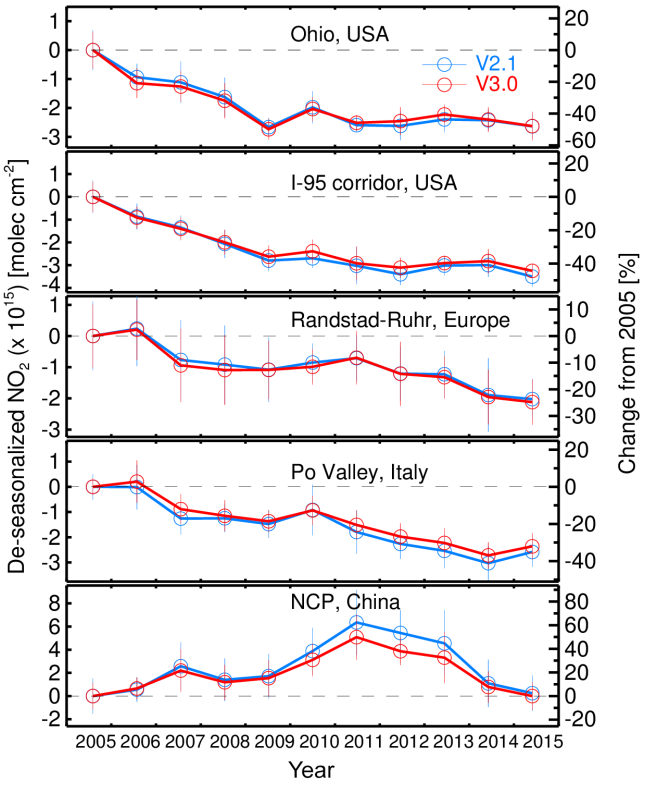

Figure 6. Annual average OMI NO_2 V_{trop} regional trends for selected regions outlined in Figs. 5 and 7–8. The regions in the eastern US and eastern China have been presented in Krotkov et al. (2016).

emissions between 2005 and 2011 over the US and western Europe, and an increase over China. The observed difference in NO_2 profiles between the two simulations could also arise from the changes in model resolution.

4.1 Impact on regional trends

Regional V_{trop} maps and trends comparing OMI NO_2 from SPv2 and SPv3 are shown in Figs. 5–8. Figure 5 shows annual average V_{trop} in 2005, 2010, and 2015 over the eastern US for both versions as well as their differences. We see reductions up to $\sim 2 \times 10^{15}$ molec. cm^{-2} over mostly polluted megacity regions in the eastern US along Interstate 95 (I-95) from Baltimore to New York (I-95 corridor, red box in Fig. 5). Elsewhere, the reductions are less than 10^{15} molec. cm^{-2}, including major industrial regions with coal-burning power plants in southwest Pennsylvania and the Ohio River valley (blue box in Fig. 5).

A signature of the change in model resolution can be seen in the difference map as subtle box-like artifacts. The significant NO_2 reduction with time is also evident. The reduction is a result of emission regulations on power plants and vehicles (Duncan et al., 2013; de Foy et al., 2015; Lamsal et al., 2015; Lu et al., 2015; Russell et al., 2012; Tong et al., 2015).

Figure 6 compares relative changes in V_{trop} in 2005–2015 for the I-95 and Ohio regions calculated from the two versions and other polluted regions discussed later. The relative trends are largely the same using both versions. NO_2 concentrations over polluted regions in the eastern US fell by more than 40 %, as result of the Clean Air Act Amendments and follow-up regulations (Krotkov et al., 2016).

Figure 7 compares annual mean tropospheric NO_2 over western Europe in 2005, 2010, and 2015. One may notice large differences in $V_{trop} \sim 2$–3×10^{15} molec. cm^{-2} over densely populated and industrialized regions in southwest Netherlands, northwest Belgium, Westphalia in Germany (Randstad-Ruhr in Fig. 6, blue box in Fig. 7), and along the industrial Po River valley in northern Italy (red box in Fig. 7). The changes are much smaller ($< 10^{15}$ molec. cm^{-2}) over less polluted regions. During the OMI mission we see significant NO_2 reductions with time (~ 25 % for Randstad-Ruhr and ~ 40 % for the Po River valley) related to national regulations and EU air quality directives aimed at reducing emissions from transportation and power sectors and creating a sustainable living environment (Boersma et al., 2015; Castellanos and Boersma, 2012). As seen in the I-95 and Ohio Valley samples, SPv2 and SPv3 retrieved tropospheric columns give trends that are well within statistical uncertainties of each other for both European regions (Fig. 6).

Figure 8 compares annual mean V_{trop} over eastern China in 2005, 2010, and 2015. The maximum V_{trop} values in pollution hot spots were reduced in new version, but areas with increased V_{trop} can also be seen over Yangtze and Pearl River deltas. The NO_2 plumes over the coastal regions reach much farther offshore. In densely populated areas the plumes seem to spread farther into the suburban regions. This could be the result of the increase in spatial resolution of the a priori profiles on the AMF calculation: in the lower panel, a signature of the previously much coarser grid ($2^\circ \times 2.5^\circ$) used in SPv2 can easily be seen. These changes have a direct implication for derived products, such as the top-down inference of NO_x emissions. Over highly polluted areas, NO_2 columns respond nearly linearly to NO_x emissions with a slope close to unity (Lamsal et al., 2011), suggesting that a ~ 15 % lower V_{trop} in SPv3 over eastern China will also be reflected in the inferred NO_x emissions.

The blue box in Fig. 8 outlines the region of the North China Plain (NCP), which has the world's largest NO_2 pollution, with an annual average $V_{trop} > 10^{16}$ molec. cm^{-2}. This is a result of the high density of coal-fired power plants and other industries, as well as dense traffic. The impact of the new version on NO_2 relative trends is more evident for the NCP than from the other regions considered. Figure 6 shows that over the NCP the NO_2 peaked in 2010–2011 but decreased from the peak by ~ 50 % by 2015 (Krotkov et al., 2016). The reduction is likely due to government regulations; economic slowdown; and technological improvements in limiting NO_x emissions by vehicles, industry, and power generation (de Foy et al., 2016). The new version shows a

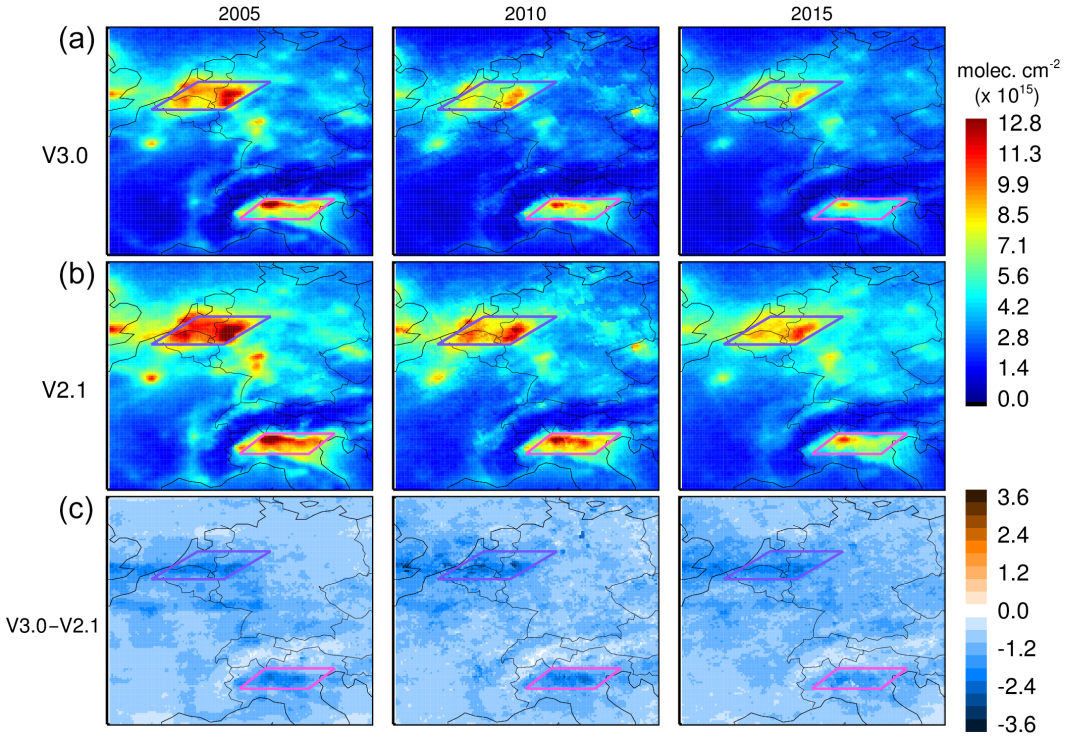

Figure 7. OMI SP V3 **(a)** and V2 **(b)** and difference V_{trop} maps over western Europe for 2005, 2010, and 2015. The boxes outline the densely populated and industrialized regions in the southwest Netherlands, northwest Belgium, and Westphalia in Germany (blue box: Randstad-Ruhr in Fig. 6), and in the industrial Po River valley in northern Italy (red box: Po Valley in Fig. 6).

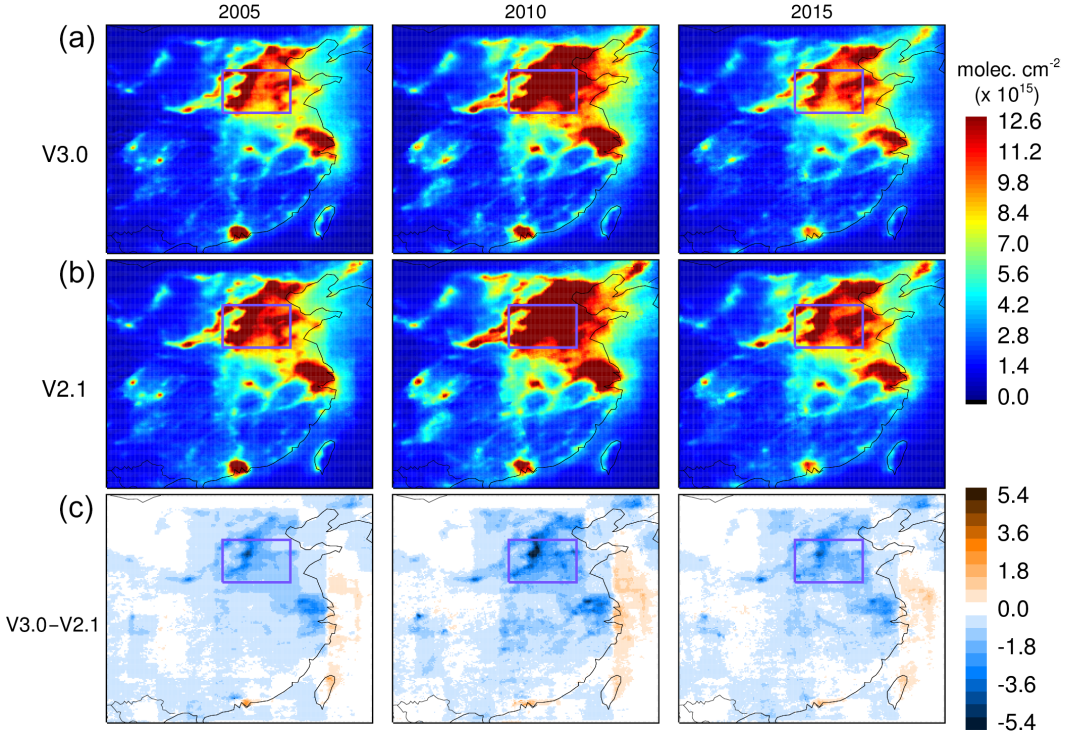

Figure 8. OMI SPv3 **(a)** and SPv2.1 **(b)** and difference V_{trop} maps **(c)** over eastern China for 2005, 2010, and 2015. The box outlines the densely populated and industrialized region in the North China Plain (NCP in Fig. 6). The region has been discussed in Krotkov et al. (2016).

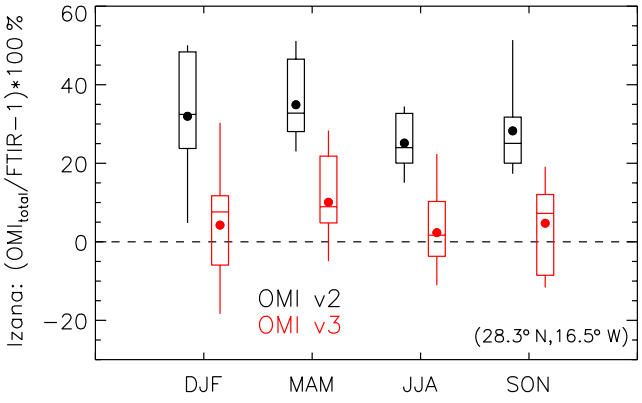

Figure 9. OMI V_{total} versus ground-based FTIR at Izana in Tenerife (28.3° N, 16.5° W), seasonally for 2005–2011. SPv2 and SPv3 are shown for FOVs within 50 km of the ground-based site. Photochemical corrections have been made for the OMI overpass time. Box-and-whisker plots show 10th, 25th, 50th, 75th, and 90th percentiles; the dots in the middle are the means.

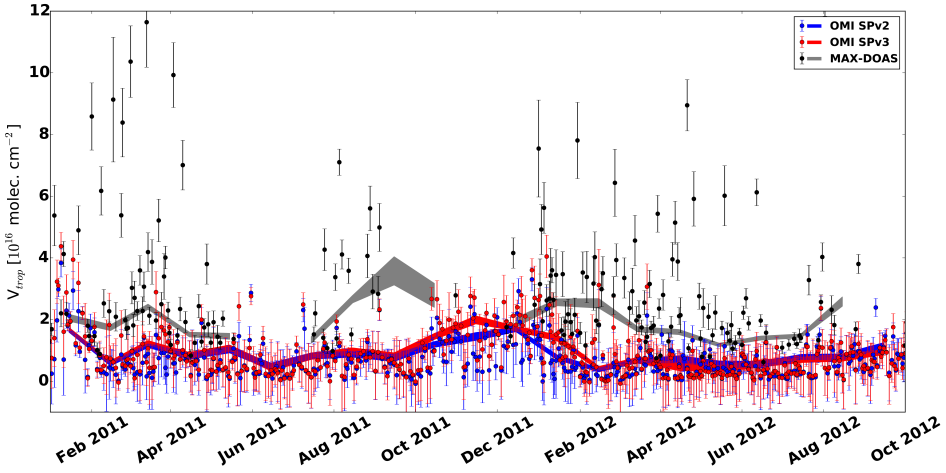

Figure 10. Comparison of OMI data with MAX-DOAS data retrieved in Hong Kong. The OMI daily data have been spatially interpolated and gridded on a 1 km × 1 km grid, and then the pixel for the measurement site has been extracted. The dots show daily values and the error bars. The lines connect monthly averages; their thickness is proportional to errors in monthly averages. Note that, compared to other parts of eastern China, V_{trop} values do not decrease significantly in SPv3 and even increase for some months, probably because of the improved a priori profiles better capturing the sharp contrast between clean ocean profiles and steep vertical gradients in one of the most densely populated cities in the world.

10–20 % smaller increase in peak NO_2 in 2010–2013 but negligible changes in early and recent years (Fig. 6).

4.2 Impact on lightning NO_x emissions estimate

Lightning-produced NO_x (LNO_x) plays an important role in tropospheric chemistry. Recent research has shown that satellite measurements are a useful tool for estimating LNO_x (Boersma et al., 2005; Beirle et al., 2010; Bucsela et al., 2010; Pickering et al., 2016). Pickering et al. (2016) combined OMI V_{trop} data with data from the World Wide Lightning Location Network (WWLLN) (Dowden et al., 2002; Lay et al., 2004; Virts et al., 2013) to estimate the production efficiency (PE) of LNO_x (moles per flash). Using SPv2 and WWLLN data from the Gulf of Mexico over five Northern Hemisphere summers (2007–2011), they obtained a mean PE value of 80 ± 45 mol flash^{-1}. Applying the same algorithm to SPv3 data, we obtain 77 ± 45 mol flash^{-1}; the difference with the SPv2 result is not statistically significant. Using the new SPv3 data will likely have little effect on LNO_x PE estimates derived in other regions.

5 Comparisons with independent measurements

We assess OMI SPv3 data by comparing with other independent observations. Here we present only initial consistency checks with other data sets. Sparse and short-term ground-

based NO_2 measurements, incomplete information, preferential placement of ground-based instruments, and the need for assessing the validation data themselves make validation of satellite NO_2 retrievals challenging and warrant detailed validation work.

5.1 Comparison with FTIR measurements in Tenerife

Figure 9 shows an improved agreement of V_{total} ($= V_{strat} + V_{trop}$) from SPv2 to SPv3 when evaluated against ground-based FTIR spectrometer measurements at Izana, Tenerife (28.3° N, 16.5° W; Schneider et al., 2005). Izana was chosen as the best candidate station in the Network for the Detection of Atmospheric Composition Change (NDACC), whose data are publicly available (http://www.ndacc.org). It is a low-to-middle-latitude site, is remote from pollution sources, makes V_{total} measurements throughout the day (not just at sunrise/sunset), and has a long data record. The FTIR measurements made before, near, and after the OMI overpass time (all solar zenith angles $< 75°$) were selected and corrected to the OMI measurement time. The seasonal mean differences with OMI SPv2 ranged from 25 to 35 %, with the OMI V_{total} always larger than the FTIR values. With SPv3, the mean differences are reduced to ~ 10 %, with OMI still higher, on average. We use the difference, $\sim 0.3 \times 10^{15}$ molec. cm^{-2}, as an estimate of the bias in V_{strat} over unpolluted, low-latitude areas (Table 2).

5.2 Comparison with MAX-DOAS measurements in Hong Kong

In previous studies, V_{trop} measured by OMI were seen to be systematically lower than multi-axis (MAX)-DOAS measurements in highly polluted "hot spots" in urban environments (Chan et al., 2012; Wenig et al., 2008). We have conducted a comparison with ground-based MAX-DOAS (tropospheric) NO_2 column measurements in the heavily polluted Hong Kong area to quantify the differences brought by the new version. The results are presented in Fig. 10. In agreement with previous studies, monthly-averaged OMI data are systematically lower than the monthly-averaged ground-based measurements but are very similar for SPv2 and SPv3. The winter values are slightly higher in the new version, bringing them closer to the MAX-DOAS data. Hong Kong is unique in that new OMI SPv3 data are close to the previous version (cf. the bottom row of panels Fig. 8). This could be due to the opposing effects of smaller SCDs and smaller AMFs due to the higher spatial resolution of the a priori NO_2 profile shapes (Fig. 3). For most other polluted locations the new SPv3 data are lower than the previous version, as confirmed with direct-sun Pandora comparisons in Helsinki (Ialongo et al., 2016). Some reasons for the discrepancies between satellite- and ground-based NO_2 retrievals include the spatial averaging inherent in the large OMI field of view; the still quite coarse sampling of the a priori profiles

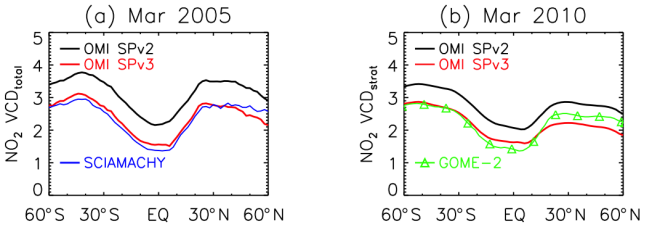

Figure 11. OMI, SCIAMACHY, and GOME-2 retrievals over the Pacific Ocean region (180–140° W) for **(a)** VCD_{total} in March 2005 and **(b)** VCD_{strat} in 2010. The SCIAMACHY and GOME-2 data have been adjusted to the local time of the OMI overpass by making photochemical corrections based on the diurnal variation simulated by the GMI CTM

and surface reflectance used for the AMF calculation; and the influence of aerosols, which have not been explicitly included in the AMF calculation. OMI shows similar annual variability to the MAX-DOAS data, and the changes made to the retrieval of the new NO_2 standard product do not significantly change the annual patterns, including derived trends.

5.3 Comparison with independent satellite retrievals

Figure 11 shows comparisons of OMI V_{total} and V_{strat} with independent satellite NO_2 data from GOME-2 (Pieter Valks, personal communication, 2013) and SCIAMACHY (Bovensmann et al., 1999) nadir measurements using the German Aerospace Center (DLR) retrievals (version 5.02) over the Pacific region for March in 2005 and 2010. The OMI data were filtered so that only FOVs unaffected by OMI's so-called row anomaly (Dobber et al., 2008) were used. The data were additionally filtered so only FOVs with a measured cloud radiance fraction of less than 0.5 were included. The Pacific region was chosen because it is relatively free of tropospheric pollution. Thus, virtually all the NO_2 column is in the stratosphere. Because stratospheric NO_2 increases largely monotonically during the day, as photochemistry repartitions nitrogen oxides (e.g., Bracher et al., 2005), observations made at different local solar times cannot be compared directly. Stratospheric NO_2 increases during the day from the time of the GOME-2 and SCIAMACHY overpasses (morning) to that of OMI (early afternoon), so the GOME-2 and SCIAMACHY data shown in Fig. 11 have been adjusted to 13:45 local time, based on the diurnal variation of NO_2 simulated by the GMI CTM. Previous version retrievals exceed both SCIAMACHY and GOME-2 by 20–30 %. The new SPv3 data are in much better agreement with the other satellite measurements, to within about 10 %, except at higher latitudes, above 50° N. These comparisons are in general agreement with the ground-based FTIR measurements in Izana (Fig. 9). The observed difference at high latitudes could arise from the difference in retrieval algorithms, instrumental behavior, or imperfect photochemical correction.

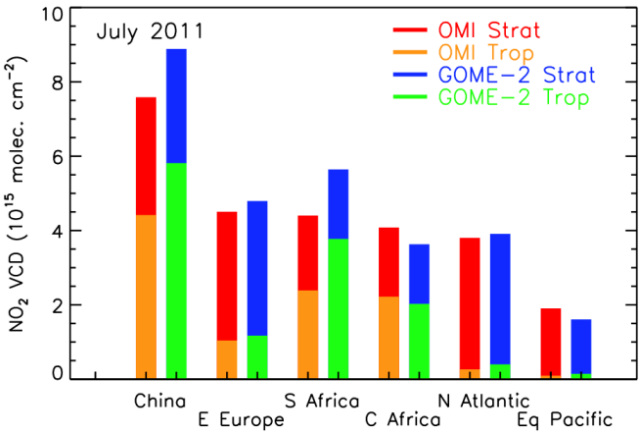

Figure 12. Mean tropospheric and stratospheric NO_2 VCDs retrieved using the new version SPv3 over several polluted and unpolluted regions: China: 110–125° E, 30-42° N; eastern Europe: 33–48° E, 42–50° N; southern Africa: 25–35° E, 22–30° S; central Africa: 10–30° E, 0–14° S; North Atlantic: 25–3° 5W, 45–51° N; and equatorial Pacific: 150–160° W, 5° S–5° N. In all cases, the GOME-2 data have been adjusted to the local time of the OMI overpass by making a photochemical correction to the stratospheric portion of the total column, based on the diurnal variation simulated by the GMI CTM.

Figure 12 shows comparisons of OMI SPv3 with GOME-2 separately for stratospheric and tropospheric VCDs. Overall, V_{strat} retrievals show better agreement, mostly well within the specified 0.5×10^{15} molec. cm^{-2}uncertainty. However, over polluted regions in eastern China and southern Africa, OMI V_{trop} fall below the GOME-2 values by 1–2×10^{15} molec. cm^{-2}. Although the retrieval algorithms for OMI (Bucsela et al., 2013) and GOME-2 (Valks et al., 2011) use a similar approach, the details of the retrievals differ quite greatly.

6 Conclusions

For the past 12 years, OMI has been making UV–Vis hyperspectral earthshine radiance measurements, including in the range 400–470 nm, where NO_2 has a strong, structured absorption feature that lends itself well to the DOAS retrieval technique. We have recently released a new version 3 OMI NO_2 standard product (SPv3) based on significant improvements in both the estimation of the NO_2 SCDs and the estimation of the AMFs. While the revised SCD estimates come from a new retrieval algorithm, the AMF refinements relate to updates in the GMI chemical and transport model inputs, primarily emission inventories and a horizontal resolution that is twice as fine in both latitude and longitude.

The quantities of greatest interest are the tropospheric, stratospheric, and total VCDs. Here we provide the uncertainties in these VCDs and evaluate the changes in the VCDs from the previous version (SPv2), also showing the improved agreement between the SPv3 VCDs and independently measured values from ground- and space-based instruments.

Over unpolluted areas V_{trop} has not changed appreciably from SPv2 to SPv3. Over more polluted areas, the V_{trop} values have typically decreased, from SPv2 to SPv3. Figure 3 shows that most of the decrease in the highly polluted areas is due to the change in SCD, with additional decrease due to the changed AMF. The V_{trop} is reduced by $2–5 \times 10^{15}$ molec. cm^{-2} over heavily polluted regions in Europe; the eastern US; and, particularly, eastern China. The relative differences between the two versions are less than $\sim 20\,\%$. With the currently adopted AMF estimates we anticipate an overall reduction in the OMI-derived top-down anthropogenic NO_x emissions and surface concentrations. However, applying a new geometry-dependent Lambertian equivalent reflectivity in AMF calculation would result in increasing tropospheric VCDs (Vasilkov et al., 2017) and derived top-down NO_x emissions and surface concentrations.

Despite large absolute differences, the relative temporal regional changes in V_{trop} as well as estimates of lightning NO_x production efficiency in free troposphere are not significantly affected in the revised data. Additional long-term ground-based column NO_2 measurements and surface concentration network data will be very helpful in validating the presented version 3 of the standard OMI NO_2 product.

Data availability. OMI NO_2 data used in this study have been publicly released as part of the Aura OMI standard NO_2 product (OMNO2.003, https://doi.org/10.5067/Aura/OMI/DATA2017) and can be obtained free of charge from the NASA Goddard Earth Sciences (GES) Data and Information Services Center's new public website: https://disc.gsfc.nasa.gov/datasets/OMNO2_V003/summary/. New OMI NO_2 overpasses as well as daily and monthly maps are available from the NASA Aura Validation Data Center website: https://avdc.gsfc.nasa.gov/. The FTIR data at Izana as part of the Network for the Detection of Atmospheric Composition Change (NDACC) are publicly available (see http://www.ndacc.org and the Aura Validation Data Center, https://avdc.gsfc.nasa.gov/).

The Supplement related to this article is available online at https://doi.org/10.5194/amt-10-3133-2017-supplement.

Competing interests. The authors declare that they have no conflict of interest.

Special issue statement. This article is part of the special issue "Ten years of Ozone Monitoring Instrument (OMI) observations (ACP/AMT inter-journal SI)". It is not associated with a conference.

Acknowledgements. We acknowledge the NASA Earth Science Division, specifically the Aura Science Team, for funding OMI NO_2 product development and analysis. The Dutch–Finnish-built OMI instrument is part of the NASA EOS Aura satellite payload. KNMI and the Netherlands Space Agency (NSO) manage the OMI project. The authors thank Susan E. Strahan for helpful discussions of the GMI model simulations.

We thank Thomas Blumenstock (Karlsruhe Institute of Technology) for help using of the Izana FTIR data. Marina Zara acknowledges support by the FP7 Project Quality Assurance for Essential Climate Variables (QA4ECV) grant no. 607405. We thank two anonymous referees for their useful suggestions that helped improve the paper.

Edited by: Alexander Kokhanovsky
Reviewed by: four anonymous referees

References

Adams, C., Normand, E. N., McLinden, C. A., Bourassa, A. E., Lloyd, N. D., Degenstein, D. A., Krotkov, N. A., Belmonte Rivas, M., Boersma, K. F., and Eskes, H.: Limb–nadir matching using non-coincident NO_2 observations: proof of concept and the OMI-minus-OSIRIS prototype product, Atmos. Meas. Tech., 9, 4103–4122, https://doi.org/10.5194/amt-9-4103-2016, 2016.

Beirle, S., Huntrieser, H., and Wagner, T.: Direct satellite observation of lightning-produced NO_x, Atmos. Chem. Phys., 10, 10965–10986, https://doi.org/10.5194/acp-10-10965-2010, 2010.

Beirle, S., Boersma, K. F., Platt, U., Lawrence, M. G., and Wagner, T.: Megacity emissions and lifetimes of nitrogen oxides probed from space, Science, 333, 1737–1739, https://doi.org/10.1126/science.1207824, 2011.

Beirle, S., Hörmann, C., Jöckel, P., Liu, S., Penning de Vries, M., Pozzer, A., Sihler, H., Valks, P., and Wagner, T.: The STRatospheric Estimation Algorithm from Mainz (STREAM): estimating stratospheric NO_2 from nadir-viewing satellites by weighted convolution, Atmos. Meas. Tech., 9, 2753–2779, https://doi.org/10.5194/amt-9-2753-2016, 2016.

Belmonte Rivas, M., Veefkind, P., Boersma, F., Levelt, P., Eskes, H., and Gille, J.: Intercomparison of daytime stratospheric NO_2 satellite retrievals and model simulations, Atmos. Meas. Tech., 7, 2203–2225, https://doi.org/10.5194/amt-7-2203-2014, 2014.

Berezin, E. V., Konovalov, I. B., Ciais, P., Richter, A., Tao, S., Janssens-Maenhout, G., Beekmann, M., and Schulze, E.-D.: Multiannual changes of CO_2 emissions in China: indirect estimates derived from satellite measurements of tropospheric NO_2 columns, Atmos. Chem. Phys., 13, 9415–9438, https://doi.org/10.5194/acp-13-9415-2013, 2013.

Boersma, K. F., Eskes, H. J., Dirksen, R. J., van der A, R. J., Veefkind, J. P., Stammes, P., Huijnen, V., Kleipool, Q. L., Sneep, M., Claas, J., Leitão, J., Richter, A., Zhou, Y., and Brunner, D.: An improved tropospheric NO_2 column retrieval algorithm for the Ozone Monitoring Instrument, Atmos. Meas. Tech., 4, 1905–1928, https://doi.org/10.5194/amt-4-1905-2011, 2011.

Boersma, K. F., Vinken, G. C. M., and Tournadre, J.: Ships going slow in reducing their NO_x emissions: changes in 2005–2012 ship exhaust inferred from satellite measurements over Europe, Environ. Res. Lett., 10, 74007, https://doi.org/10.1088/1748-9326/10/7/074007, 2015.

Bovensmann, H., Burrows, J. P., Buchwitz, M., Frerick, J., Noël, S., Rozanov, V. V., Chance, K. V., and Goede, A. P. H.: SCIAMACHY: Mission Objectives and Measurement Modes, J. Atmos. Sci., 56, 127–150, https://doi.org/10.1175/1520-0469(1999)056<0127:SMOAMM>2.0.CO;2, 1999.

Bracher, A., Sinnhuber, M., Rozanov, A., and Burrows, J. P.: Using a photochemical model for the validation of NO_2 satellite measurements at different solar zenith angles, Atmos. Chem. Phys., 5, 393–408, https://doi.org/10.5194/acp-5-393-2005, 2005.

Bucsela, E. J., Pickering, K. E. , Huntemann, T. L., Cohen, R. C., Perring, A., Gleason, J. F., Blakeslee, R. J., Albrecht, R. I., Holzworth, R., Cipriani, J. P., Vargas-Navarro, D., Mora-Segura, I., Pacheco-Hernández, A., and Sadí Laporte-Molina, S.: Lightning-generated NO_X seen by the Ozone Monitoring Instrument during NASA's Tropical Composition, Cloud and Climate Coupling Experiment (TC4), J. Geophys. Res., 115, D00J10, https://doi.org/10.1029/2009JD013118, 2010.

Bucsela, E. J., Krotkov, N. A., Celarier, E. A., Lamsal, L. N., Swartz, W. H., Bhartia, P. K., Boersma, K. F., Veefkind, J. P., Gleason, J. F., and Pickering, K. E.: A new stratospheric and tropospheric NO_2 retrieval algorithm for nadir-viewing satellite instruments: applications to OMI, Atmos. Meas. Tech., 6, 2607–2626, https://doi.org/10.5194/amt-6-2607-2013, 2013.

Burrows, J. P., Weber, M., Buchwitz, M., Rozanov, V., and Ladst, A.: The Global Ozone Monitoring Experiment (GOME): Mission Concept and First Scientific Results, J. Atmos. Sci., 56, 151–175, https://doi.org/10.1175/1520-0469(1999)056<0151:TGOMEG>2.0.CO;2, 1999.

Callies, J., Corpaccioli, E., Eisinger, M., Hahne, A., and Lefebvre, A.: GOME-2 – Metop's second-generation sensor for operational ozone monitoring, ESA Bulletin-European Space Agency, 102, 28–36, 2000.

Castellanos, P. and Boersma, K. F.: Reductions in nitrogen oxides over Europe driven by environmental policy and economic recession,, Scientific Reports, 2, 265, https://doi.org/10.1038/srep00265, 2012.

Chan, K. L., Pöhler, D., Kuhlmann, G., Hartl, A., Platt, U., and Wenig, M. O.: NO_2 measurements in Hong Kong using LED based long path differential optical absorption spectroscopy, Atmos. Meas. Tech., 5, 901–912, https://doi.org/10.5194/amt-5-901-2012, 2012.

Chance, K., Kurosu, T. P., and Sioris, C. E.: Undersampling correction for array detector-based satellite spectrometers, Appl. Optics, 44, 1296, https://doi.org/10.1364/AO.44.001296, 2005.

Chance, K. V. and Spurr, R. J. D.: Ring effect studies: Rayleigh scattering, including molecular parameters for rotational Raman scattering, and the Fraunhofer spectrum, Appl. Optics, 36, 5224–5230, https://doi.org/10.1364/AO.36.005224, 1997.

Chin, M., Diehl, T., Tan, Q., Prospero, J. M., Kahn, R. A., Remer, L. A., Yu, H., Sayer, A. M., Bian, H., Geogdzhayev, I. V., Holben, B. N., Howell, S. G., Huebert, B. J., Hsu, N. C., Kim, D., Kucsera, T. L., Levy, R. C., Mishchenko, M. I., Pan, X., Quinn, P. K., Schuster, G. L., Streets, D. G., Strode, S. A., Torres, O., and Zhao, X.-P.: Multi-decadal aerosol variations from 1980 to 2009: a perspective from observations and a global model, Atmos. Chem. Phys., 14, 3657–3690, https://doi.org/10.5194/acp-14-3657-2014, 2014.

Curier, R. L., Kranenburg, R., Segers, A. J. S., Timmermans, R. M. A., and Schaap, M.: Synergistic use of OMI NO_2 tropospheric columns and LOTOS–EUROS to evaluate the NO_x emission trends across Europe, Remote Sens. Environ., 149, 58–69, https://doi.org/10.1016/j.rse.2014.03.032, 2014.

Dave, J. V.: Multiple Scattering in a Non-Homogeneous, Rayleigh Atmosphere, J. Atmos. Sci., 22, 273–279, 1965.

de Foy, B., Wilkins, J. L., Lu, Z., Streets, D. G., and Duncan, B. N.: Model evaluation of methods for estimating surface emissions and chemical lifetimes from satellite data, Atmos. Environ., 98, 66–77, https://doi.org/10.1016/j.atmosenv.2014.08.051, 2014.

de Foy, B., Lu, Z., Streets, D. G., Lamsal, L. N., and Duncan, B. N.: Estimates of power plant NO_x emissions and lifetimes from OMI NO_2 satellite retrievals, Atmos. Environ., 116, 1–11, https://doi.org/10.1016/j.atmosenv.2015.05.056, 2015.

de Foy, B., Lu, Z., and Streets, D. G.: Satellite NO_2 retrievals suggest China has exceeded its NO_x reduction goals from the twelfth Five-Year Plan, Scientific Reports, 6, 35912, https://doi.org/10.1038/srep35912, 2016.

DeLand, M. and Marchenko, S.: The solar chromospheric Ca and Mg indices from Aura OMI, J. Geophys. Res.-Atmos., 118, 3415–3423, https://doi.org/10.1002/jgrd.50310, 2013.

Ding, J., van der A, R. J., Mijling, B., Levelt, P. F., and Hao, N.: NO_x emission estimates during the 2014 Youth Olympic Games in Nanjing, Atmos. Chem. Phys., 15, 9399–9412, https://doi.org/10.5194/acp-15-9399-2015, 2015.

Dobber, M., Kleipool, Q., Dirksen, R., Levelt, P., Jaross, G., Taylor, S., Kelly, T., Flynn, L., Leppelmeier, G., and Rozemeijer, N.: Validation of Ozone Monitoring Instrument level 1b data products, J. Geophys. Res., 113, D15S06, https://doi.org/10.1029/2007JD008665, 2008.

Dobber, M. R., Dirksen, R. J., Levelt, P. F., Oord, G. H. J. Van Den, Voors, R. H. M., Kleipool, Q., Jaross, G., Kowalewski, M., Hilsenrath, E., Leppelmeier, G. W., Vries, J. D. V. J. De, Dierssen, W., and Rozemeijer, N. C.: Ozone monitoring instrument calibration, IEEE T. Geosci. Remote, 44, 1209–1238, https://doi.org/10.1109/TGRS.2006.869987, 2006.

Dowden, R. J., Brundell, J. B., and Rodger. C. J.: VLF lightning location by time of group arrival (TOGA) at multiple sites, J. Atmos. Sol.-Terr. Phys., 64, 817–830, 2002.

Duncan, B. N., Strahan, S. E., Yoshida, Y., Steenrod, S. D., and Livesey, N.: Model study of the cross-tropopause transport of biomass burning pollution, Atmos. Chem. Phys., 7, 3713–3736, https://doi.org/10.5194/acp-7-3713-2007, 2007.

Duncan, B. N., Yoshida, Y., de Foy, B., Lamsal, L. N., Streets, D. G., Lu, Z., Pickering, K. E., and Krotkov, N. A.: The observed response of Ozone Monitoring Instrument (OMI) NO_2 columns to NO_x emission controls on power plants in the United States: 2005–2011, Atmos. Environ., 81, 102–111, https://doi.org/10.1016/j.atmosenv.2013.08.068, 2013.

Duncan, B. N., Prados, A. I., Lamsal, L. N., Liu, Y., Streets, D. G., Gupta, P., Hilsenrath, E., Kahn, R. A., Nielsen, J. E., Beyersdorf, A. J., Burton, S. P., Fiore, A. M., Fishman, J., Henze, D. K., Hostetler, C. A., Krotkov, N. A., Lee, P., Lin, M., Pawson, S., Pfister, G., Pickering, K. E., Pierce, R. B., Yoshida, Y., and Ziemba, L. D.: Satellite data of atmospheric pollution for U.S. air quality applications: Examples of applications, summary of data end-user resources, answers to FAQs, and common mistakes to avoid, Atmos. Environ., 94, 647–662, https://doi.org/10.1016/j.atmosenv.2014.05.061, 2014.

Duncan, B. N., Lamsal, L. N., Thompson, A. M., Yoshida, Y., Lu, Z., Streets, D. G., Hurwitz, M. M. and Pickering, K. E.: A space-based, high-resolution view of notable changes in urban NO_x pollution around the world (2005–2014), J. Geophys. Res.-Atmos., 121, 976–996, https://doi.org/10.1002/2015JD024121, 2016.

Eskes, H. J. and Boersma, K. F.: Averaging kernels for DOAS total-column satellite retrievals, Atmos. Chem. Phys., 3, 1285–1291, https://doi.org/10.5194/acp-3-1285-2003, 2003.

Fioletov, V. E., McLinden, C. A., Krotkov, N., and Li, C.: Lifetimes and emissions of SO_2 from point sources estimated from OMI, Geophys. Res. Lett., 42, 1969–1976, https://doi.org/10.1002/2015GL063148, 2015.

Ghude, S. D., Pfister, G. G., Jena, C., Van Der A, R. J., Emmons, L. K., and Kumar, R.: Satellite constraints of nitrogen oxide (NO_x) emissions from India based on OMI observations and WRF-Chem simulations, Geophys. Res. Lett., 40, 423–428, https://doi.org/10.1029/2012GL053926, 2013.

Goldberg, D. L., Lamsal, L. N., Loughner, C. P., Lu, Z., and Streets, D. G.: A high-resolution and observationally constrained OMI NO_2 satellite retrieval, Atmos. Chem. Phys. Discuss., https://doi.org/10.5194/acp-2017-219, in review, 2017.

Grainger, J. F. and Ring, J.: Anomalous Fraunhofer Line Profiles, Nature, 193, p. 762, https://doi.org/10.1038/193762a0, 1962.

Herman, J., Cede, A., Spinei, E., Mount, G., Tzortziou, M., and Abuhassan, N.: NO_2 column amounts from ground-based Pandora and MFDOAS spectrometers using the direct-sun DOAS technique: Intercomparisons and application to OMI validation, J. Geophys. Res.-Atmos., 114, D13307, https://doi.org/10.1029/2009JD011848, 2009.

Hönninger, G., von Friedeburg, C., and Platt, U.: Multi axis differential optical absorption spectroscopy (MAX-DOAS), Atmos. Chem. Phys., 4, 231–254, https://doi.org/10.5194/acp-4-231-2004, 2004.

Hsu, J. and Prather, M. J.: Global long-lived chemical modes excited in a 3-D chemistry transport model: Stratospheric N_2O, NO_y, O_3 and CH_4 chemistry, Geophys. Res. Lett., 37, L07805, https://doi.org/10.1029/2009GL042243, 2010.

Ialongo, I., Herman, J., Krotkov, N., Lamsal, L., Boersma, K. F., Hovila, J., and Tamminen, J.: Comparison of OMI NO_2 observations and their seasonal and weekly cycles with ground-based measurements in Helsinki, Atmos. Meas. Tech., 9, 5203–5212, https://doi.org/10.5194/amt-9-5203-2016, 2016.

Jacob, D. J., Heikes, E. G., Fan, S.-M., Logan, J. A., Mauzerall, D. L., Bradshaw, J. D., Singh, H. B., Gregory, G. L., Talbot, R. W., Blake, D. R., and Sachse, G. W.: Origin of ozone and NO_x in the tropical troposphere: A photochemical analysis of aircraft observations over the South Atlantic basin, J. Geophys. Res.-Atmos., 101, 24235–24250, https://doi.org/10.1029/96JD00336, 1996.

Jaeglé, L., Martin, R. V., Chance, K., Steinberger, L., Kurosu, T. P., Jacob, D. J., Modi, A. I., Yoboué, V., Sigha-Nkamdjou, L., and Galy-Lacaux, C.: Satellite mapping of rain-induced nitric oxide emissions from soils, J. Geophys. Res.-Atmos., 109, D21310, https://doi.org/10.1029/2004JD004787, 2004.

Joiner, J., Bhartia, P. K., Cebula, R. P., Hilsenrath, E., McPeters, R. D., and Park, H.: Rotational Raman scattering (Ring effect) in

satellite backscatter ultraviolet measurements, Appl. Optics, 34, 4513, https://doi.org/10.1364/AO.34.004513, 1995.

Konovalov, I. B., Beekmann, M., Richter, A., and Burrows, J. P.: Inverse modelling of the spatial distribution of NO_x emissions on a continental scale using satellite data, Atmos. Chem. Phys., 6, 1747–1770, https://doi.org/10.5194/acp-6-1747-2006, 2006.

Konovalov, I. B., Beekmann, M., Richter, A., Burrows, J. P., and Hilboll, A.: Multi-annual changes of NO_x emissions in megacity regions: nonlinear trend analysis of satellite measurement based estimates, Atmos. Chem. Phys., 10, 8481–8498, https://doi.org/10.5194/acp-10-8481-2010, 2010.

Konovalov, I. B., Berezin, E. V., Ciais, P., Broquet, G., Zhuravlev, R. V., and Janssens-Maenhout, G.: Estimation of fossil-fuel CO_2 emissions using satellite measurements of "proxy" species, Atmos. Chem. Phys., 16, 13509–13540, https://doi.org/10.5194/acp-16-13509-2016, 2016.

Krotkov, N. A., McLinden, C. A., Li, C., Lamsal, L. N., Celarier, E. A., Marchenko, S. V., Swartz, W. H., Bucsela, E. J., Joiner, J., Duncan, B. N., Boersma, K. F., Veefkind, J. P., Levelt, P. F., Fioletov, V. E., Dickerson, R. R., He, H., Lu, Z., and Streets, D. G.: Aura OMI observations of regional SO_2 and NO_2 pollution changes from 2005 to 2015, Atmos. Chem. Phys., 16, 4605–4629, https://doi.org/10.5194/acp-16-4605-2016, 2016.

Kuhlmann, G., Hartl, A., Cheung, H. M., Lam, Y. F., and Wenig, M. O.: A novel gridding algorithm to create regional trace gas maps from satellite observations, Atmos. Meas. Tech., 7, 451–467, https://doi.org/10.5194/amt-7-451-2014, 2014.

Kuhlmann, G., Lam, Y. F., Cheung, H. M., Hartl, A., Fung, J. C. H., Chan, P. W., and Wenig, M. O.: Development of a custom OMI NO_2 data product for evaluating biases in a regional chemistry transport model, Atmos. Chem. Phys., 15, 5627–5644, https://doi.org/10.5194/acp-15-5627-2015, 2015.

Lamsal, L. N., Martin, R. V., Van Donkelaar, A., Celarier, E. A., Bucsela, E. J., Boersma, K. F., Dirksen, R., Luo, C., and Wang, Y.: Indirect validation of tropospheric nitrogen dioxide retrieved from the OMI satellite instrument: Insight into the seasonal variation of nitrogen oxides at northern midlatitudes, J. Geophys. Res.-Atmos., 115, D05302, https://doi.org/10.1029/2009JD013351, 2010.

Lamsal, L. N., Martin, R. V., Padmanabhan, A., van Donkelaar, A., Zhang, Q., Sioris, C. E., Chance, K., Kurosu, T. P., and Newchurch, M. J.: Application of satellite observations for timely updates to global anthropogenic NO_x emission inventories, Geophys. Res. Lett., 38, L05810, https://doi.org/10.1029/2010GL046476, 2011.

Lamsal, L. N., Krotkov, N. A., Celarier, E. A., Swartz, W. H., Pickering, K. E., Bucsela, E. J., Gleason, J. F., Martin, R. V., Philip, S., Irie, H., Cede, A., Herman, J., Weinheimer, A., Szykman, J. J., and Knepp, T. N.: Evaluation of OMI operational standard NO_2 column retrievals using in situ and surface-based NO_2 observations, Atmos. Chem. Phys., 14, 11587–11609, https://doi.org/10.5194/acp-14-11587-2014, 2014.

Lamsal, L. N., Duncan, B. N., Yoshida, Y., Krotkov, N. A., Pickering, K. E., Streets, D. G., and Lu, Z.: U.S. NO_2 trends (2005–2013): EPA Air Quality System (AQS) data versus improved observations from the Ozone Monitoring Instrument (OMI), Atmos. Environ., 110, 130–143, https://doi.org/10.1016/j.atmosenv.2015.03.055, 2015.

Laughner, J. L., Zare, A., and Cohen, R. C.: Effects of daily meteorology on the interpretation of space-based remote sensing of NO_2, Atmos. Chem. Phys., 16, 15247–15264, https://doi.org/10.5194/acp-16-15247-2016, 2016.

Lay, E. H., Holzworth, R. H., Rodger, C. J., Thomas, J. N., Pinto, O., and Dowden, R. L.: WWLL global lightning detection system: Regional validation study in Brazil, Geophys. Res. Lett., 31, L03102, https://doi.org/10.1029/2003GL018882, 2004.

Levelt, P. F., Hilsenrath, E., Leppelmeier, G. W., Oord, G. H. J. Van Den, Bhartia, P. K., Tamminen, J., Haan, J. F., De and Veefkind, J. P.: Science Objectives of the Ozone Monitoring Instrument, IEEE T. Geosci. Remote, 44, 1199–1208, 2006a.

Levelt, P. F., Oord, G. H. J. Van Den, Dobber, M. R., Mälkki, A., Visser, H., Vries, J. De, Stammes, P., Lundell, J. O. V., and Saari, H.: The Ozone Monitoring Instrument, IEEE T. Geosci. Remote 44, 1093–1101, 2006b.

Lin, J.-T., Martin, R. V., Boersma, K. F., Sneep, M., Stammes, P., Spurr, R., Wang, P., Van Roozendael, M., Clémer, K., and Irie, H.: Retrieving tropospheric nitrogen dioxide from the Ozone Monitoring Instrument: effects of aerosols, surface reflectance anisotropy, and vertical profile of nitrogen dioxide, Atmos. Chem. Phys., 14, 1441–1461, https://doi.org/10.5194/acp-14-1441-2014, 2014.

Liu, F., Zhang, Q., van der A, R. J., Zheng, B., Tong, D., Yan, L., Zheng, Y., and He, K.: Recent reduction in NO_x emissions over China: synthesis of satellite observations and emission inventories, Environ. Res. Lett., 11, 114002, https://doi.org/10.1088/1748-9326/11/11/114002, 2016.

Lorente, A., Folkert Boersma, K., Yu, H., Dörner, S., Hilboll, A., Richter, A., Liu, M., Lamsal, L. N., Barkley, M., De Smedt, I., Van Roozendael, M., Wang, Y., Wagner, T., Beirle, S., Lin, J.-T., Krotkov, N., Stammes, P., Wang, P., Eskes, H. J., and Krol, M.: Structural uncertainty in air mass factor calculation for NO_2 and HCHO satellite retrievals, Atmos. Meas. Tech., 10, 759–782, https://doi.org/10.5194/amt-10-759-2017, 2017.

Lu, Z. and Streets, D. G.: Increase in NO_x emissions from Indian thermal power plants during 1996–2010: unit-based inventories and multisatellite observations, Environ. Sci. Technol., 46, 7463–70, https://doi.org/10.1021/es300831w, 2012.

Lu, Z., Streets, D. G., de Foy, B., Lamsal, L. N., Duncan, B. N., and Xing, J.: Emissions of nitrogen oxides from US urban areas: estimation from Ozone Monitoring Instrument retrievals for 2005–2014, Atmos. Chem. Phys., 15, 10367–10383, https://doi.org/10.5194/acp-15-10367-2015, 2015.

Marchenko, S., Krotkov, N. A., Lamsal, L. N., Celarier, E. A., Swartz, W. H., and Bucsela, E. J.: Revising the slant column density retrieval of nitrogen dioxide observed by the Ozone Monitoring Instrument, J. Geophys. Res.-Atmos., 120, 5670–5692, https://doi.org/10.1002/2014JD022913, 2015.

Marchenko, S. V. and DeLand, M. T.: Solar Spectral Irradiance changes during cycle 24, Astrophys. J., 789, 117, https://doi.org/10.1088/0004-637X/789/2/117, 2014.

Martin, R. V., Chance, K., Jacob, D. J., Kurosu, T. P., Spurr, R. J. D., Bucsela, E., Gleason, J. F., Palmer, P. I., Bey, I., Fiore, A. M., Li, Q., Yantosca, R. M., and Koelemeijer, R. B. A.: An improved retrieval of tropospheric nitrogen dioxide from GOME, J. Geophys. Res., 107, 4437, https://doi.org/10.1029/2001JD001027, 2002.

Martin, R. V., Sioris, C. E., Chance, K., Ryerson, T. B., Bertram, T. H., Wooldridge, P. J., Cohen, R. C., Neuman, J. A., Swanson, A., and Flocke, F. M.: Evaluation of space-based constraints on global nitrogen oxide emissions with regional aircraft measurements over and downwind of eastern North America, J. Geophys. Res., 111, D15308, https://doi.org/10.1029/2005JD006680, 2006.

McLinden, C. A., Fioletov, V., Krotkov, N. A., Li, C., Boersma, K. F., and Adams, C.: A Decade of Change in NO_2 and SO_2 over the Canadian Oil Sands As Seen from Space, Environ. Sci. Technol., 50, 331–337, https://doi.org/10.1021/acs.est.5b04985, 2016.

Mijling, B. and Van Der A, R. J.: Using daily satellite observations to estimate emissions of short-lived air pollutants on a mesoscopic scale, J. Geophys. Res.-Atmos., 117, 1–20, https://doi.org/10.1029/2012JD017817, 2012.

Nowlan, C. R., Martin, R. V., Philip, S., Lamsal, L. N., Krotkov, N. A., Marais, E. A., Wang, S., and Zhang, Q.: Global dry deposition of nitrogen dioxide and sulfur dioxide inferred from space-based measurements, Global Biogeochem. Cy., 28, 1025–1043, https://doi.org/10.1002/2014GB004805, 2014.

Palmer, P. I., Jacob, D. J., Chance, K., Martin, R. V., Spurr, R. J. D., Kurosu, T. P., Bey, I., Yantosca, R, Fiore, A., and Li, Q.: Air mass factor formulation for spectroscopic measurements from satellites: Application to formaldehyde retrievals from the Global Ozone Monitoring Experiment, J. Geophys. Res., 106, 14539–14550, https://doi.org/10.1029/2000JD900772, 2001.

Pickering, K. E., Bucsela, E., Allen, D., Ring, A., Holzworth, R., and Krotkov, N. A.: Estimates of lightning NOx production based on OMI NO_2 observations over the Gulf of Mexico, J. Geophys. Res.-Atmos., 121, 8668–8691, https://doi.org/10.1002/2015JD024179, 2016.

Platt, U. and Stutz, J.: Differential Optical Absorption Spectroscopy, Physics of Earth and Space Environments, Springer, Berlin, Germany, https://doi.org/10.1007/978-3-540-75776-4, 2008.

Reuter, M., Buchwitz, M., Hilboll, A., Richter, A., Schneising, O., Hilker, M., Heymann, J., Bovensmann, H., and Burrows, J. P.: Decreasing emissions of NO_x relative to CO_2 in East Asia inferred from satellite observations, Nat. Geosci., 7, 792–795, https://doi.org/10.1038/ngeo2257, 2014.

Richter, A., Eyring, V., Burrows, J. P., Bovensmann, H., Lauer, A., Sierk, B., and Crutzen, P. J.: Satellite measurements of NO_2 from international shipping emissions, Geophys. Res. Lett., 31, 1–4, https://doi.org/10.1029/2004GL020822, 2004.

Richter, A., Burrows, J. P., Nüss, H., Granier, C., and Niemeier, U.: Increase in tropospheric nitrogen dioxide over China observed from space, Nature, 437, 129–132, https://doi.org/10.1038/nature04092, 2005.

Rienecker, M. M., Suarez, M. J., Gelaro, R., Todling, R., Bacmeister, J., Liu, E., Bosilovich, M. G., Schubert, S. D., Takacs, L., Kim, G.-K., Bloom, S., Chen, J., Collins, D., Conaty, A., da Silva, A., Gu, W., Joiner, J., Koster, R. D., Lucchesi, R., Molod, A., Owens, T., Pawson, S., Pegion, P., Redder, C. R., Reichle, R., Robertson, F. R., Ruddick, A. G., Sienkiewicz, M., Woollen, J., Rienecker, M. M., Suarez, M. J., Gelaro, R., Todling, R., Julio Bacmeister, Liu, E., Bosilovich, M. G., Schubert, S. D., Takacs, L., Kim, G.-K., Bloom, S., Chen, J., Collins, D., Conaty, A., Silva, A. da, Gu, W., Joiner, J., Koster, R. D., Lucchesi, R., Molod, A., Owens, T., Pawson, S., Pegion, P., Redder, C. R., Reichle, R., Robertson, F. R., Ruddick, A. G., Sienkiewicz, M., and Woollen, J.: MERRA: NASA's Modern-Era Retrospective Analysis for Research and Applications, J. Climate, 24, 3624–3648, https://doi.org/10.1175/JCLI-D-11-00015.1, 2011.

Russell, A. R., Perring, A. E., Valin, L. C., Bucsela, E. J., Browne, E. C., Wooldridge, P. J., and Cohen, R. C.: A high spatial resolution retrieval of NO_2 column densities from OMI: method and evaluation, Atmos. Chem. Phys., 11, 8543–8554, https://doi.org/10.5194/acp-11-8543-2011, 2011.

Russell, A. R., Valin, L. C., and Cohen, R. C.: Trends in OMI NO_2 observations over the United States: effects of emission control technology and the economic recession, Atmos. Chem. Phys., 12, 12197–12209, https://doi.org/10.5194/acp-12-12197-2012, 2012.

Schenkeveld, V. M. E., Jaross, G., Marchenko, S., Haffner, D., Kleipool, Q. L., Rozemeijer, N. C., Veefkind, J. P., and Levelt, P. F.: In-flight performance of the Ozone Monitoring Instrument, Atmos. Meas. Tech., 10, 1957–1986, https://doi.org/10.5194/amt-10-1957-2017, 2017.

Schneider, M., Blumenstock, T., Chipperfield, M. P., Hase, F., Kouker, W., Reddmann, T., Ruhnke, R., Cuevas, E., and Fischer, H.: Subtropical trace gas profiles determined by ground-based FTIR spectroscopy at Izaña (28° N, 16° W): Five-year record, error analysis, and comparison with 3-D CTMs, Atmos. Chem. Phys., 5, 153–167, https://doi.org/10.5194/acp-5-153-2005, 2005.

Schoeberl, M. R., Douglass, A. R., Hilsenrath, E., Bhartia, P. K., Beer, R., Waters, J. W., Gunson, M. R., Froidevaux, L., Gille, J. C., Barnett, J. J., Levelt, P. F., and DeCola, P.: Overview of the EOS aura mission, IEEE T. Geosci. Remote, 44, 1066–1072, https://doi.org/10.1109/TGRS.2005.861950, 2006.

Seinfeld, J. H. and Pandis, S. N.: Atmospheric Chemistry and Physics: From Air Pollution to Climate Change, John Wiley & Sons Inc, New York, 1998.

Shindell, D. T., Faluvegi, G., Koch, D. M., Schmidt, G. A., Unger, N., and Bauer, S. E.: Improved Attribution of Climate Forcing to Emissions, Science, 326, 716–718, https://doi.org/10.1126/science.1174760, 2009.

Sneep, M., de Haan, J. F., Stammes, P., Wang, P., Vanbauce, C., Joiner, J., Vasilkov, A. P., and Levelt, P. F.: Three-way comparison between OMI and PARASOL cloud pressure products, J. Geophys. Res., 113, 1–11, https://doi.org/10.1029/2007JD008694, 2008.

Spinei, E., Cede, A., Swartz, W. H., Herman, J., and Mount, G. H.: The use of NO_2 absorption cross section temperature sensitivity to derive NO_2 profile temperature and stratospheric–tropospheric column partitioning from visible direct-sun DOAS measurements, Atmos. Meas. Tech., 7, 4299–4316, https://doi.org/10.5194/amt-7-4299-2014, 2014.

Stammes, P., Sneep, M., de Haan, J. F., Veefkind, J. P., Wang, P., and Levelt, P. F.: Effective cloud fractions from the Ozone Monitoring Instrument: Theoretical framework and validation, J. Geophys. Res.-Atmos., 113, 1–12, https://doi.org/10.1029/2007JD008820, 2008.

Stavrakou, T., Müller, J. F., Boersma, K. F., De Smedt, I., and van der A, R. J.: Assessing the distribution and growth rates of NO_x emission sources by inverting a 10-year record of NO_2 satellite columns, Geophys. Res. Lett., 35, L10801, https://doi.org/10.1029/2008GL033521, 2008.

Strahan, S. E., Douglass, A. R., and Newman, P. A.: The contributions of chemistry and transport to low arctic ozone in March 2011 derived from Aura MLS observations, J. Geophys. Res.-Atmos., 118, 1563–1576, https://doi.org/10.1002/jgrd.50181, 2013.

Streets, D. G., Canty, T., Carmichael, G. R., de Foy, B., Dickerson, R. R., Duncan, B. N., Edwards, D. P., Haynes, J. A., Henze, D. K., Houyoux, M. R., Jacob, D. J., Krotkov, N. A., Lamsal, L. N., Liu, Y., Lu, Z., Martin, R. V., Pfister, G. G., Pinder, R. W., Salawitch, R. J., and Wecht, K. J.: Emissions estimation from satellite retrievals: A review of current capability, Atmos. Environ., 77, 1011–1042, https://doi.org/10.1016/j.atmosenv.2013.05.051, 2013.

Strode, S. A., Rodriguez, J. M., Logan, J. A., Cooper, O. R., Witte, J. C., Lamsal, L. N., Damon, M., Van Aartsen, B., Steenrod, S. D., and Strahan, S. E.: Trends and variability in surface ozone over the United States, J. Geophys. Res.-Atmos., 120, 9020–9042, https://doi.org/10.1002/2014JD022784, 2015.

Tong, D. Q., Lamsal, L., Pan, L., Ding, C., Kim, H., Lee, P., Chai, T., Pickering, K. E., and Stajner, I.: Long-term NO_x trends over large cities in the United States during the great recession: Comparison of satellite retrievals, ground observations, and emission inventories, Atmos. Environ., 107, 70–84, https://doi.org/10.1016/j.atmosenv.2015.01.035, 2015.

US EPA: Nitrogen Dioxide (NO_2) Pollution, available at: https://www.epa.gov/no2-pollution, last access: 11 February 2017.

Valks, P., Pinardi, G., Richter, A., Lambert, J.-C., Hao, N., Loyola, D., Van Roozendael, M., and Emmadi, S.: Operational total and tropospheric NO_2 column retrieval for GOME-2, Atmos. Meas. Tech., 4, 1491–1514, https://doi.org/10.5194/amt-4-1491-2011, 2011.

van der A, R. J., Mijling, B., Ding, J., Koukouli, M. E., Liu, F., Li, Q., Mao, H., and Theys, N.: Cleaning up the air: effectiveness of air quality policy for SO_2 and NO_x emissions in China, Atmos. Chem. Phys., 17, 1775–1789, https://doi.org/10.5194/acp-17-1775-2017, 2017.

van Geffen, J. H. G. M., Boersma, K. F., Van Roozendael, M., Hendrick, F., Mahieu, E., De Smedt, I., Sneep, M., and Veefkind, J. P.: Improved spectral fitting of nitrogen dioxide from OMI in the 405–465 nm window, Atmos. Meas. Tech., 8, 1685–1699, https://doi.org/10.5194/amt-8-1685-2015, 2015.

Vasilkov, A., Qin, W., Krotkov, N., Lamsal, L., Spurr, R., Haffner, D., Joiner, J., Yang, E.-S., and Marchenko, S.: Accounting for the effects of surface BRDF on satellite cloud and trace-gas retrievals: a new approach based on geometry-dependent Lambertian equivalent reflectivity applied to OMI algorithms, Atmos. Meas. Tech., 10, 333–349, https://doi.org/10.5194/amt-10-333-2017, 2017.

Vasilkov, A. P.: Ocean Raman scattering in satellite backscatter UV measurements, Geophys. Res. Lett., 29, 1837, https://doi.org/10.1029/2002GL014955, 2002.

Vasilkov, A. P., Joiner, J., Oreopoulos, L., Gleason, J. F., Veefkind, P., Bucsela, E., Celarier, E. A., Spurr, R. J. D., and Platnick, S.: Impact of tropospheric nitrogen dioxide on the regional radiation budget, Atmos. Chem. Phys., 9, 6389–6400, https://doi.org/10.5194/acp-9-6389-2009, 2009.

Vinken, G. C. M., Boersma, K. F., Maasakkers, J. D., Adon, M., and Martin, R. V.: Worldwide biogenic soil NO_x emissions inferred from OMI NO_2 observations, Atmos. Chem. Phys., 14, 10363–10381, https://doi.org/10.5194/acp-14-10363-2014, 2014.

Virts, K. S., Wallace, J. M., Hutchins, M. L., and Holzworth, R. H.: Highlights of a new ground-based, hourly global lightning climatology, B. Am. Meteorol. Soc., 94, 1381–1392, 2013.

Wenig, M. O., Cede, A. M., Bucsela, E. J., Celarier, E. A., Boersma, K. F., Veefkind, J. P., Brinksma, E. J., Gleason, J. F., and Herman, J. R.: Validation of OMI tropospheric NO_2 column densities using direct-Sun mode Brewer measurements at NASA Goddard Space Flight Center, J. Geophys. Res.-Atmos., 113, D16S45, https://doi.org/10.1029/2007JD008988, 2008.

Zara, M., Boersma, K. F., van Geffen, J., Eskes, H. J., Veefkind, J. P., Sneep, M., De Smedt, I., Van Roozendael, M., Richter, A., Peters, E., Wagner, T., Beirle, S., Marchenko, S. V., Krotkov, N. A., Celarier, E. A., and Lamsal, L. N.: Quality assurance for NASA, KNMI, and QA4ECV spectral fitting algorithms for OMI NO_2 slant columns, EOS Aura Science Team Meeting, 30 August, available at: https://avdc.gsfc.nasa.gov/index.php?site=1072744097 (last access: 13 July 2017), 2016.

Zhang, Q., Streets, D. G., He, K., Wang, Y., Richter, A., Burrows, J. P., Uno, I., Jang, C. J., Chen, D., Yao, Z., and Lei, Y.: NO_x emission trends for China, 1995–2004: The view from the ground and the view from space, J. Geophys. Res.-Atmos., 112, D22306, https://doi.org/10.1029/2007JD008684, 2007.

Zhou, Y., Brunner, D., Hueglin, C., Henne, S., and Staehelin, J.: Changes in OMI tropospheric NO_2 columns over Europe from 2004 to 2009 and the influence of meteorological variability, Atmos. Environ., 46, 482–495, https://doi.org/10.1016/j.atmosenv.2011.09.024, 2012.